Characterizing distinct components of tactical aircraft noise sources

David F. Van Komen, Blaine M. Harker, Tracianne B. Neilsen, Kent L. Gee, S. Hales Swift, Alan T. Wall, J. Micah Downing, and Michael M. James

Citation: The Journal of the Acoustical Society of America **147**, 3550 (2020); doi: 10.1121/10.0001260
View online: https://doi.org/10.1121/10.0001260
View Table of Contents: https://asa.scitation.org/toc/jas/147/5
Published by the Acoustical Society of America

JASA ARTICLE

Characterizing distinct components of tactical aircraft noise sources

David F. Van Komen,[1,a)] Blaine M. Harker,[1] Tracianne B. Neilsen,[1,b)] Kent L. Gee,[1,c)] S. Hales Swift,[1] Alan T. Wall,[2] J. Micah Downing,[3] and Michael M. James[3]

[1]*Department of Physics and Astronomy, Brigham Young University, Provo, Utah 84602, USA*

[2]*Battlespace Acoustics Branch, Air Force Research Laboratory, Wright-Patterson AFB, Ohio 45433, USA*

[3]*Blue Ridge Research and Consulting, LLC, Asheville, North Carolina 28801, USA*

ABSTRACT:

Noise from a tactical aircraft can impact operations due to concerns regarding military personnel noise exposure and community annoyance and disturbance. The efficacy of mission planning can increase when the distinct, complex acoustic source mechanisms creating the noise are better understood. For each type of noise, equivalent acoustic source distributions are obtained from a tied-down F-35B operating at various engine conditions using the hybrid method for acoustic source imaging of Padois, Gauthier, and Berry [J. Sound Vib. **333**, 6858–6868 (2014)]. The source distributions for the distinct noise types are obtained using different sections of a 71 element, ground-based linear array. Using a subarray close to the nozzle exit plane, source distributions are obtained for fine-scale turbulent mixing noise and broadband shock-associated noise, although grating lobes complicate interpretations at higher frequencies. Results for a subarray spanning the maximum sound region show that the multiple frequency peaks in tactical aircraft noise appear to originate from overlapping source regions. The observation of overlapping spatial extent of competing noise sources is supported by the coherence properties of the source distributions for the different subarrays. © *2020 Acoustical Society of America*. https://doi.org/10.1121/10.0001260

(Received 30 December 2019; revised 24 April 2020; accepted 28 April 2020; published online 18 May 2020)

[Editor: D. Keith Wilson] Pages: 3550–3564

I. INTRODUCTION

Noise from high-performance, tactical aircraft affect military operations, such as training tempos; the potential risk of hearing damage and community annoyance and disturbance can lead to operational restrictions. Distinct types of noise are generated by the turbulent structures and shock cells in the aircraft exhaust, such as fine- and large-scale turbulent mixing noise (TMN) and broadband shock-associated noise (BBSAN). The contribution of these distinct types of noise on the sound field varies with spatial location and operating condition. Increased understanding of these different noise sources can help inform operational decisions that can reduce the effects of the noise on military personnel and surrounding communities, as well as inform future noise reduction efforts. This paper presents equivalent acoustic source distributions for different noise sources from the F-35B at multiple engine power conditions.

Two primary types of jet noise are TMN and BBSAN. In the two-source model for TMN,[1,2] large-scale turbulent structures generate partially correlated, directional noise, responsible for the dominant radiation in the aft direction, and fine-scale turbulent structures produce uncorrelated, omnidirectional radiation, which can be detected outside the maximum radiation region and, particularly, to the sideline of the peak source region. Fine-scale similarity (FSS) and large-scale similarity (LSS) spectra were derived from laboratory-scale jet noise by Tam *et al.*[1,3] Neilsen *et al.* applied these similarity spectra to noise from the F-35B[4] and another high-performance military aircraft[5] and found good agreement with a few exceptions, including at high frequencies where nonlinear propagation was believed to be present and at frequencies and positions affected by multiple spatiospectral lobes. The other main type of noise from the F-35B is BBSAN, which is present in nonideally expanded, supersonic jets.[6–12] The F-35 BBSAN was analyzed in Refs. 4 and 13. BBSAN is the loudest component of the F-35B in the region to the side and forward of the nozzle exit plane.[13] Both TMN and BBSAN are identifiable in the F-35B noise field,[4] but an increased understanding of the underlying sources is needed to inform military operations and guide noise reduction efforts.

Many methods have been employed to estimate equivalent acoustic source distributions for TMN and BBSAN. Equivalent acoustic source distributions for TMN have primarily been obtained in laboratory-scale environments, e.g., by the sound power[14] and via vector acoustic intensity.[15] The resulting equivalent acoustic source distributions compliment studies that focus on the physics of turbulence and flow, such as particle image velocimetry (PIV)[16] or computational fluid dynamics (CFD),[17,18] by providing a means of comparing predictions of acoustic radiation.[19] Indirect estimates of

[a)]Electronic mail: david.vankomen@gmail.com, ORCID: 0000-0003-0610-0806.

[b)]ORCID: 0000-0002-9729-373X.

[c)]ORCID: 0000-0002-5768-6483.

 0001-4966/2020/147(5)/3550/15/$30.00

https://doi.org/10.1121/10.0001260

equivalent acoustic source distributions can be obtained from phased-array methods.[18,20,21] The current study applies a phased-array method, called the hybrid method for acoustic source imaging by Padois *et al.*[22] (hereafter referred to as HM), to sound measured in different spatial regions near a tied-down F-35B to obtain unique equivalent acoustic source distributions for different sources of jet noise.

Phased-array methods have been utilized to estimate equivalent acoustic source distributions for jet noise. For example, acoustical holography and traditional beamforming methods have been applied to both laboratory-scale jet noise[23–27] and tactical aircraft noise[28–33] to estimate the overall levels of sources. However, traditional beamforming relies on the assumption that extended noise sources can be represented by a distribution of incoherent monopoles[20,34] processed independently—an assumption not met by the extended, partially correlated sources present in jet noise.[1,2] To overcome such limitations, advanced phased-array methods have been developed, many of which are reviewed in Refs. 18, 20, 21, and 35. Methods for localizing correlated and partially correlated noise sources include DAMAS-C[36] and derivatives,[37] covariance matrix fitting for correlated sources [CMF-C[38] and mapping of acoustic correlated sources (MACS)[38,39]], the source directivity modeling of a cross spectral matrix method for modeling source directivity,[40] noise source localization and optimization of phased-array results modified for coherent sources,[41] generalized inverse beamforming[42] (L_1-GIB) and its derivatives [such as the generalized inverse (GINV) beamforming method[43] and generalized weighted inverse beamforming[44,45]], and the HM.[22] Such phased-array techniques have been applied to both single-flow[46] and dual-flow[25] hot, laboratory-scale jets. These algorithms produce a complex, source cross-spectral matrix (SCSM)[37] representation of the underlying source distribution that not only represents equivalent source levels but also provides information about the source's self-coherence. These results can provide a more complete equivalent source distribution to give insights into the complicated sound radiation mechanisms for tactical aircraft noise, provided the measurement array is sufficient.

In attempting to isolate different noise sources, different types of arrays may be used. For example, Brusniak *et al.*[47] employed multiple arrays (such as a polar array, multiple parallel linear arrays, and a multi-arm spiral) to measure the various jet noise sources of a commercial grade engine that propagate in different directions of the sound field. By using traditional beamforming, they found that the linear array was most appropriate to estimate TMN properties of full-scale, tactical aircraft. Underbrink[48] introduced an array concept called "pletharray," which is a measurement array that contains a plethora of subarrays, and demonstrated that such arrays work well in instances that require directional noise and sufficiently show large-picture results for signal processing. Dougherty,[43] when developing the GINV method, transformed his results into an angular-aperture-independent coordinate system to mitigate the effects of small array aperture sizes. In each of these cases, smaller arrays placed in strategic locations were more useful for isolating different selections of noise, although the ideal array geometry generally includes large numbers of microphones and depends mainly on the noise of interest.

A recent study on tactical aircraft noise, conducted by Harker *et al.*,[49] presents equivalent source distributions found using the HM. Noise measured on a 50-element, ground-based microphone array spanning 30 m in the vicinity of a tied-down, tactical aircraft was input to the HM. Equivalent source distributions were obtained for one-third octave (OTO) bands (spanning 40–2000 Hz). Source distributions for the higher frequencies were attainable because of a phase unwrapping and interpolation method called UPAINT, developed by Goates *et al.*[50] From each complex SCSM, the self-coherence of the source reconstructions was calculated, and predicted OTO levels were compared to measured levels both closer to and farther from the input array. In Ref. 49, the HM was used to obtain meaningful equivalent acoustic sources for the overall field. Because the entire array was used and only OTO levels were presented, TMN dominated the source reconstruction, and BBSAN was not observed.

By contrast, the present study uses the HM to develop equivalent acoustic source distributions for different components of F-35B noise, which contains stronger BBSAN. For comparison, the HM is first applied to noise measured using all 71 elements of a ground-based, linear array that spanned 32 m near the F-35B to obtain equivalent overall source distributions for 3 engine power conditions, similar to those shown in Harker *et al.*[49] but for a different aircraft. To further characterize the overall equivalent acoustic source, the source self-coherence is shown and a nondimensionalized coherence length is introduced to analyze frequency-independent trends. (A concept explained in Sec. IV B that was not presented previously.)

To accomplish the task of localizing distinct components of jet noise, namely BBSAN and TMN sources, the HM is applied to different subsets of the full array. These subarrays are selected to cover upstream, middle, and downstream regions relative to the jet flow as described in Sec. IV C. The upstream subarray detects primarily BBSAN and fine-scale TMN. The center subarray covers the spatial area in which multiple spectral peaks are present in the measured spectra.[5] The downstream subarray is dominated by one low-frequency peak[51–53] similar to that postulated for large-scale TMN. The resulting equivalent acoustic sources and nondimensionalized coherence lengths for the three subarrays are compared across engine condition and frequency to provide insights into where various noise types, such as BBSAN and TMN, originate. Of particular interest is how the source localizations from different subarrays appear to overlap both physically and spectrally. Each of these analyses help create a more detailed picture regarding the different noise sources present in high-performance military aircraft noise.

II. METHODS

A previous numerical study involving jet noise simulated via wavepackets conducted by Harker *et al.*[35]

compared various advanced phased-array methods, such as cross beamforming,[54] functional beamforming,[34] the HM,[22] the GINV method,[43] and the MACS[39] method, and found that all methods adequately estimated source levels using a distributed numerical source at multiple frequency bands within 6 dB upon reconstruction for the scenarios tested. However, they concluded that the HM showed improved overall performance while estimating source levels, as well as coherence properties, to within an adequate threshold at the array design frequency. The HM was also found to reduce noise along the outer edges of the reconstruction ranges. Following these conclusions, Harker*et al.*[35] applied the HM to tactical aircraft noise to obtain the first OTO band equivalent acoustic source distributions that account for source coherence. For the current study, source reconstructions from the HM and GINV beamforming method are compared and confirm these observations. These methods are briefly discussed in Sec. II A.

This discussion of the methods is followed (in Sec. II B) by an explanation of how the results depend on the input array and describes how a subarray analysis is used to investigate potential source regions for BBSAN and TMN from the F-35B. Sources of uncertainty due to array selection are also presented.

A. Techniques

A variety of phased-array methods has been developed to estimate equivalent acoustic source distribution for radiated sound. These methods typically solve an inverse problem and use a regularization technique. The input to the inverse problem for many phased-array problems in acoustics is a linear set of equations formulated to estimate radiating sources in the vicinity of an array of sensors located at positions x_i, with $i = 1, \ldots, m$. Assuming a total of s possible sources, the equivalent source reconstructions at positions $\{\vec{r}_i\}$ can be found by solving a least-squares minimization problem with measurement points: $\mathbf{P} = \mathbf{G}\mathbf{q}$, where the vector array of acoustic pressures, $\mathbf{p}$, for a given frequency, f, is $[m, 1]$ in size, with m being the number of microphones. The matrix $\mathbf{G}$ is the Green function matrix comprising the steering vectors along the columns such that $\mathbf{G} = [\mathbf{g}_1 \ldots \mathbf{g}_s]$ and models the free-field propagation from each source location to each microphone array element. Each steering vector, $\mathbf{g}_i$, is comprised of steering elements from the potential source location, $\vec{r}_i$, to each measurement location. The vector of complex source strengths, $\mathbf{q}$, is $[s, 1]$ in size, where s is the number of potential source locations. These source strengths are combined to form the SCSM, defined as $\mathbf{C} \equiv \mathbf{q}\mathbf{q}^{\mathrm{H}}$, whose diagonal elements provide complex source volume velocity estimates at positions $\{\vec{r}_i\}$ in units of m^3/s for the F-35B noise discussed in this paper.

Many different techniques exist to solve for $\mathbf{q}$, but a common method is to employ a Moore-Penrose pseudoinverse coupled with a regularization approach.[22,55] Traditional Tikhonov regularization improves the conditioning of $\mathbf{G}^{\mathrm{H}}\mathbf{G}$ with a penalization parameter along the diagonal entries determined by various means, such as Morozov discrepancy and generalized cross validation.[56] In the HM, the regularization is accomplished by expanding the solution through the use of *a priori* information obtained from the conventional beamforming (CBF) method. In a departure from the spatially independent approach used in Tikhonov regularization, the use of this *a priori* information in the regularization weights the Green function matrix differently across the source reconstruction region. This spatially dependent penalization allows the noise threshold to vary in space as a function of the precomputed CBF levels so that regions where acoustic sources are absent are more strongly regularized. A more in-depth review of the HM's mathematics can be found in Refs. 49 and 35. Chapter 2 of Ref. 35 provides the regularization parameters used in the current study.

Because regularization can impact the results, initial HM results are compared with those obtained by the GINV[42] method in Sec. IV A. The GINV method, developed by Suzuki[42] and expanded upon by Dougherty,[43] is useful because it can be applied to both incoherent and coherent source distributions. Instead of looking for a least-squares solution to find $\mathbf{q}$, Suzuki solved a more generalized cost function by means of an L_1 norm parameter, which solves the problem using an iteratively reweighted least square (IRLS) algorithm. Dougherty, however, moved away from the L_1 norm using a singular-value decomposition, improving the speed of the algorithm. These methods are summarized in Refs. 42 and 43, respectively. The GINV method relies on reciprocation, which amplifies small noises—generally associated with the measurement floor.

All inverse techniques have the potential to under-regularize (allows more resolution at the cost of extra noise) or over-regularize (lower resolution causes excessive smoothing) the results. In this work, the regularization parameter and other methodologies employed are described in chapter 2 of Ref. 35. The comparison of the GINV method and the HM results at a few frequencies is shown in Sec. IV A. Consistency between the results from the GINV method and the HM applied to a small subset of the data increases confidence in the source distributions obtained from the HM.

B. Subarrays analyses

While the GINV method and the HM both adequately overcome the limitation of incoherent monopole distribution as the underlying model associated with traditional beamforming, careful implementation of these methods is required to obtain equivalent acoustic source distributions and coherence properties for distinct sources of jet noise. The spatiospectral variation in the types of noise present needs to be accounted for; some regions are dominated by large- or fine-scale TMN and others are dominated by BBSAN. The noise received on the input array determines the information contained in the beamforming source reconstructions. Thus, the source approximation results obtained from using a long input array that spans a broad angular

https://doi.org/10.1121/10.0001260

range differs from that obtained when portions of the array (namely, subarrays) are used; the full array can be divided in subarrays to create equivalent source reconstructions for the different components of jet noise. A suitably small array may still capture the dominant features of a particular region of interest. (Details about the subarray selection are explained in Sec. IV C with beamforming results presented in Secs. IV D and IV E)

Because the large-scale TMN and BBSAN radiate primarily in different directions, sound measured in different spatial regions can yield equivalent source distributions for each. However, selecting subarrays and analyzing their resulting equivalent source distributions requires an understanding of potential sources of uncertainty. For example, frequency and array aperture are tied directly to resolution. At low frequencies, the reduced apparent array aperture increases the beam width of the array and leads to erroneously large source reconstruction as the energy is spread across larger regions. This spreading is evident in the results in Sec. IV and imposes a lower frequency limit on source characterization. The second consideration deals with the quantity of microphones used in the calculations. Both the HM and the GINV method are, at their core, matrix optimization problems, so fewer microphones in the subarrays (compared to the full array) leads to fewer data points in the source matrix, which produces a larger uncertainty in the source reconstructions than if more microphones had sampled the same region. Another consideration is experimental error (in array location, source presupposed location, timing, etc.), which is amplified under an inverse operation. Thus, subarray results operate effectively for a different frequency band compared with those of the entire array, and they provide a unique perspective on the equivalent source reconstructions. These inherent uncertainties must be remembered when comparing beamforming results from the full array to those from the subarrays results as in Secs. IV D and IV E.

III. MEASUREMENT DETAILS

A series of measurements was taken at various engine conditions to create equivalent source distributions that provide insight into overlapping source regions for the F-35B. The measurement setup is detailed in Sec. III A, showing the positioning of the aircraft as well as microphones used in both full array beamforming and subarray beamforming. Section III B shows spectral maps for three different engine conditions. Features of interest are also noted before the measurements are input to the beamforming algorithms, the results of which are discussed in Sec. IV.

A. Measurements

The noise measurements used in this study were obtained from a tied-down F-35B at Edwards Air Force Base in 2013. The aircraft, equipped with a Pratt and Whitney F135-PW-600 afterburning turbofan engine (capable of up to 43 000 lb of thrust; East Hartford, CT), was tied down to a concrete run-up pad while the engine was operated at different engine thrust requests (ETRs)—the only parameter known to the authors for describing the engine operating conditions and related jet parameters (see Ref. 57, Sec. 3b)—ranging from idle (13% ETR) to 150% ETR. (ETR values greater than 100% indicate afterburning conditions.) The nozzle of the engine was located 2.0 m above the ground and had a nominal diameter of 1 m, although the exact nozzle diameter varied with the engine condition. Measurements were conducted in early morning hours when temperatures varied between 19.4 °C and 23.1 °C, relative humidity varied between 37.6% and 45.7%, and an average wind speed of 3.3 kn was present. The sound speed was calculated from the temperature and humidity measured at the time of each recording.

Microphones were arranged in either line arrays or semicircular arcs that were centered at the microphone array reference point (MARP) as described by Wall *et al.*[51] The MARP represents a rough estimate of the apparent source location for the dominant TMN at many frequencies of interest and is used to define angles relative to the engine inlet. The coordinate system used in this paper, illustrated in Fig. 1, has its origin at the nozzle exit plane with the jet centerline along the positive z axis. The term "downstream" refers to the region with larger z values. The horizontal distance away from the jet centerline is the x axis, and the height from the ground is the positive y axis. The MARP is located at $z = 7.5$ m. The measurement system was originally laid out to the left side of the aircraft as seen in the study by James *et al.*,[58] although in this study, for ease of plotting and consistency with previous studies on the F-35, all plots are mirrored to place the array on the right side of the aircraft.

While over 350 microphones were placed in the vicinity of the F-35B, this study focuses on a linear ground-based array. This linear array includes 71 elements [0.45 inter-element spacing with 6.35 mm (1/4 in.) diameter microphones] located parallel to and 8–10 m from the estimated shear layer. The linear array spans 32 m, which corresponds to an angular aperture of 35°–152° relative to the engine inlet and the MARP as illustrated in Fig. 1. Calibrated acoustic pressure waveform data were simultaneously acquired with

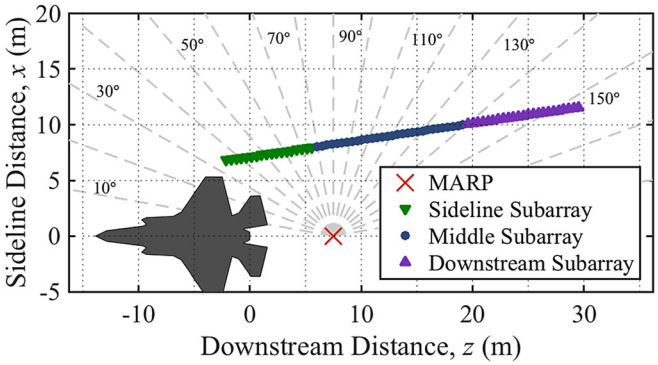

FIG. 1. (Color online) Measurement array setup for the F-35 B. The "×" is the MARP located 7.5 m behind the nozzle of the aircraft. This figure also indicates the division of the microphones into subarrays described in Sec. IV C.

National Instruments PXI-4498 cards (Austin, TX) with a 204.8 kHz sampling rate for 30 s on each test. Although five or six measurements were taken at each ETR, the variation in the measured levels was less than 1 dB,[13] so only one measurement for each ETR was used for this study. Placing the array on the ground removes complications due to ground reflections. By positioning the array approximately parallel to the jet shear layer, the risk of unwanted effects from the turbulent pressure fluctuations of the jet hydrodynamic near field was minimized. Ground effects on the sound speed or waveform were not included, which is a reasonable approximation due to the short propagation distance.

B. Spectral levels

The variation of the radiated sound signals recorded across the linear array is shown as spectral maps in Fig. 2. The sound pressure level (SPL) for each microphone is shown for (a) 75%, (b) 100%, and (c) 150% ETR. The horizontal axis is the z position of the microphones or the distance relative to the nozzle exit plane as seen in Fig. 1. These spectral maps also include vertical lines showing how the microphones were divided into subarrays as discussed in Sec. IV C. These data at various ETRs[58] have been used for correlation and coherence analyses,[52] acoustical holography,[53] BBSAN variation,[13,59] and nonlinear propagation effects.[60]

Features to note in these spectral maps include BBSAN signatures (present as streaks near and above 400 Hz for $z < 5$ m at each ETR) as well as multiple spatiospectral lobes (present as 4–5 lighter regions beyond $z = 5$ m starting at 100 Hz that shift positions as frequency increases). These distinct features in the spectral maps prompted the division of the full array into subarrays to separate out these features. The subarray to the left (noted as sideline subarray in Fig. 1), captures the BBSAN signature at each ETR while avoiding the large and dominating lobes at larger z. The other two sections (noted as the middle subarray and downstream subarray in Fig. 1) contain noise likely dominated by TMN, although the current understanding of TMN does not allow for multiple spectral peaks seen in tactical aircraft engine noise.[5,61,62] The middle and downstream subarrays are divided shortly after the lobe centered at 200 Hz. The complex spectra corresponding to these different spatial regions compose the **p** vector used in the beamforming algorithms discussed in Sec. II B.

Prior to the phased-array analyses, the measured spectra are preprocessed to produce a cross-spectral matrix at each frequency. Each measurement was divided into time-waveform blocks of 16 384 samples each with a 50% overlap. Each block was filtered by a Hann window, and then the Fourier transform of each block was calculated. The resulting spectra were multiplied to yield the cross spectrum of each measurement pair per block, which were then averaged together. The resulting complex spectra were next averaged to create the time-averaged, cross-spectral density matrix, **C** at each frequency. These **C** are used in the GINV method

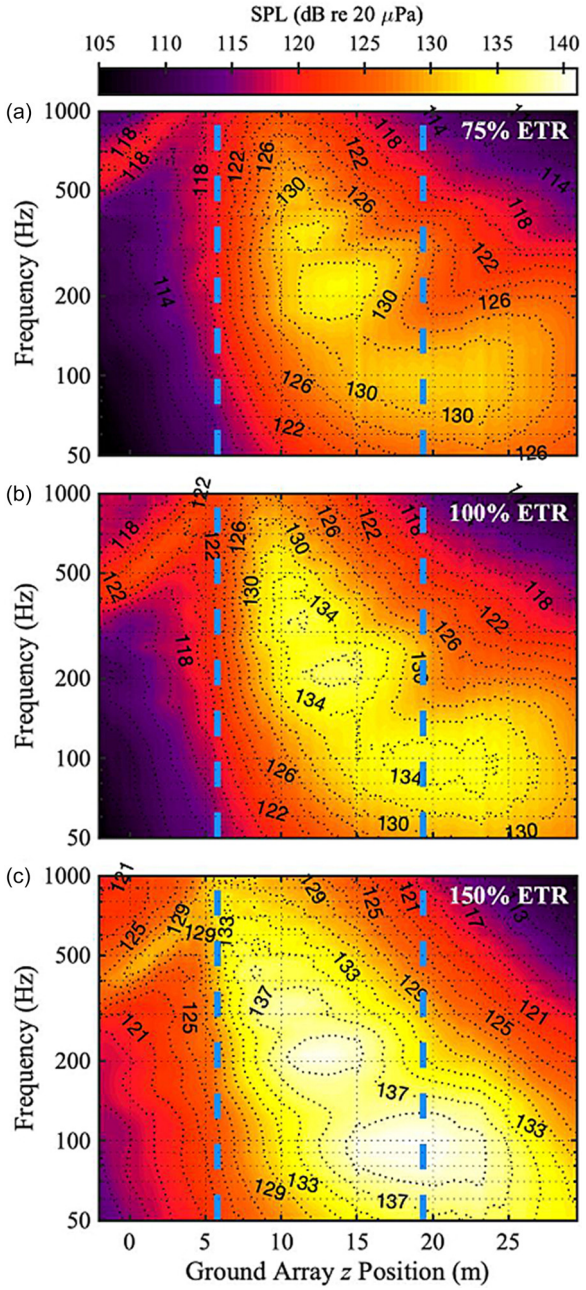

FIG. 2. (Color online) Spatiospectral narrowband maps of sound pressure level (SPL) on the microphone array as a function of frequency and distance from the nozzle (z) for three different ETRs. The small black dotted lines represent the SPL at 2 dB intervals. The bold, dashed lines represent the division of the array into subarrays used in Secs. IV C–IV E.

and the HM to calculate source reconstructions. Each scanning location (i.e., equivalent source location), $\vec{r}_i$, or scanning grid location selected for the equivalent source reconstructions was at the jet centerline at nozzle height: a horizontal line located at $y = 2$ m and $x = 0$ m.

Phased-array methods produce grating lobes when attempting reconstructions above the spatial Nyquist frequency due to spatial aliasing. With an array spacing of approximately 0.5 m, the expected Nyquist frequency is near 380 Hz for the linear array. However, given the positioning of the array at an angle relative to the direction of

https://doi.org/10.1121/10.0001260

incidence, the effective Nyquist frequency is observed to be closer to 500 Hz.

IV. RESULTS

The goal of this study is to obtain equivalent acoustic source distributions for tactical aircraft noise that provide insight into the apparent source regions of the different types of noise sources and could be used for sound field predictions. In Sec. IV A, a comparison between the results from the HM and GINV method is provided to motivate the use of the HM to obtain equivalent source representations. In Sec. IV B, the HM results using the entire linear array are presented, which provide an equivalent model for the combined noise sources. Section IV C provides a brief discussion on the subarray selection procedure, explaining which types of noise sources are expected to appear in which results with localization of BBSAN presented in Sec. IV D and TMN presented in Sec. IV E. The noise source characteristics are confirmed by nondimensionalized coherence length analysis, which helps estimate the source properties given by the resulting beamforming matrix at various frequencies. The ultimate goal of each analysis is to identify and characterize equivalent source distributions for BBSAN and TMN from the F-35B operating at different engine conditions.

A. Comparison of the HM and the GINV method

Because matrix optimizations like the HM require a user-defined regularization parameter, a quick comparison is done between the HM and the GINV method to check for consistency. A comparison of the results from the HM and the GINV method applied to F-35B data at three frequencies from the full array is shown in Fig. 3. The diagonals of the resulting source SCSM contain the source strengths as a function of position along the axis. Because different reconstruction grid spacing is used at different frequencies, the source strength values are normalized by the grid spacing to remove dependence on the spacing of source reconstructions.[35,49] The resulting frequency-dependent source strength densities are plotted as a function of the centerline position (z) downstream, where $z = 0$ is at the nozzle exit plane. Examples of source strength densities found for 100, 250, and 400 Hz at 150% ETR are shown in Fig. 3. Both the GINV method and the HM provide consistent results over approximately the top 12 dB of the results in both level (within 1–2 dB) and shape. The consistency of the two methods over the top 12 dB of the source reconstructions provides confidence in the results in the rest of the paper. In the numerical studies shown in chapter 2 of Harker,[35] the HM results were less sensitive to the regularization than the GINV method. Thus, the HM is selected for the remaining analyses in this paper.

B. Full array results

Source strength densities for individual frequencies (as in Fig. 3) can be combined to produce maps to more easily visualize trends. The source strength densities from the HM as a function of centerline position and frequency at three engine conditions (a) 75%, (b) 100%, and (c) 150% ETR are shown in Fig. 4. The plots (as well as the similar plots in Secs. IV C–IV E) have been overlaid with white contour lines showing absolute levels and black contour lines displaying levels relative to the peak value at each frequency. Specifically, the −6 and −12 dB relative level contours are useful to examine the frequency variation in the spatial

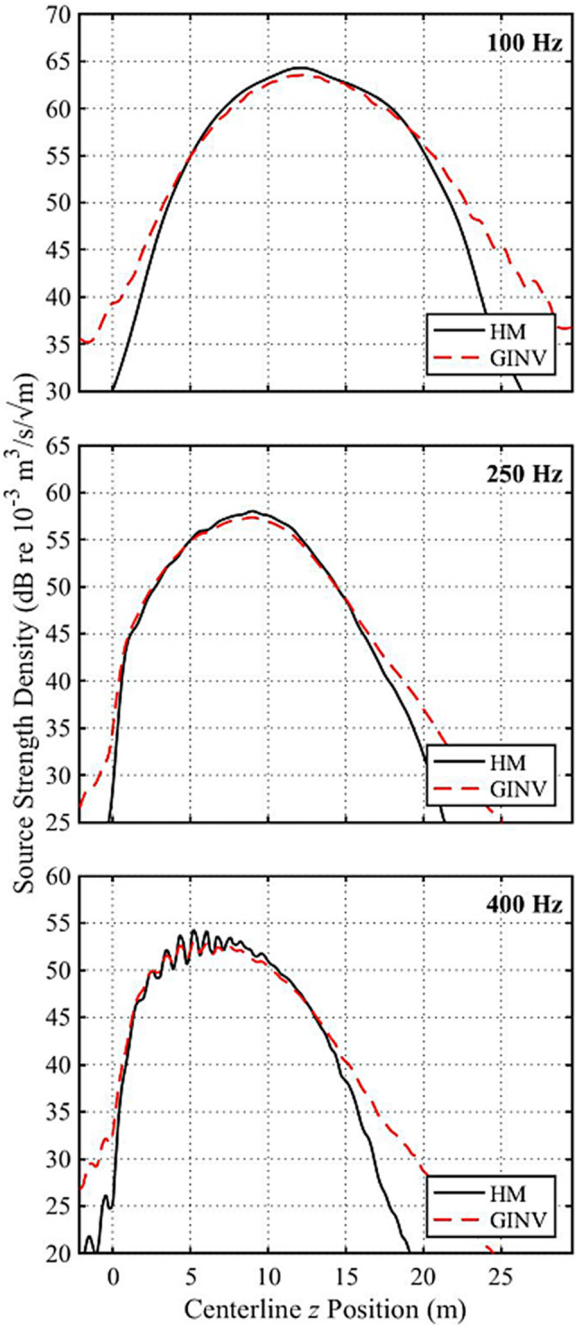

FIG. 3. (Color online) Source strength densities, where **q** represents the diagonals of the SCSM along the jet centerline z position for the F-35B at 150% ETR. The solid line represents the results from the HM, while the dashed line represents the results from the generalized inverse (GINV) method.

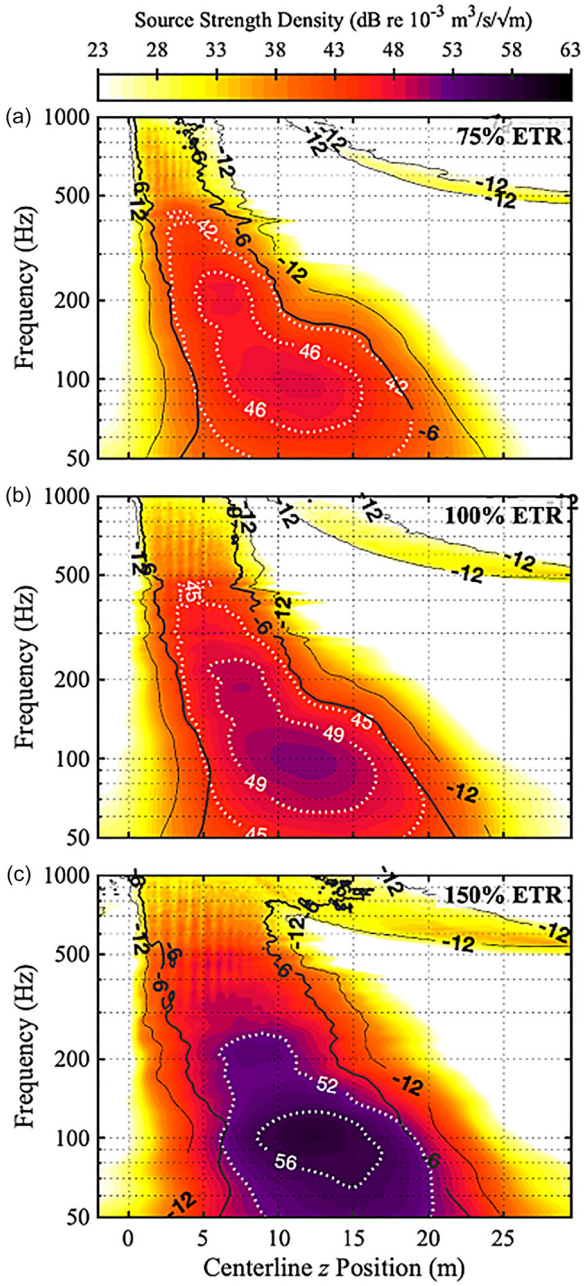

FIG. 4. (Color online) Source strength density (diagonal of SCSM) for the F-35 B along the jet centerline z position as a function of frequency using the full array at (a) 75%, (b) 100%, and (c) 150% ETR. The colormap and dotted contour lines indicate absolute levels, and the solid contour lines indicate the levels relative to the maximum level at each frequency.

distribution. For example, in Fig. 4(a), the 75% ETR part [, at 100 Hz, the 6 dB-down region covers 5–18 m, whereas at 200 Hz, the 6 dB-down region covers a narrower spatial aperture of approximately 3–10 m.

As mentioned previously in Sec. III B, grating lobes begin to appear around 500 Hz for $z > 10$ m and cause the source strength densities to decrease rapidly in the higher frequency regions as the HM algorithm distributes energy, which should belong in the main lobe, into the additional grating lobes. The size and level of the span of the grating lobes increases with ETR, but the same general characteristics of size and positioning are present in all cases. The uncertainty introduced by the grating lobes was studied by Harker *et al.*[49] in obtaining source strength densities for a different tactical aircraft. When the UPAINT method[50] was used to remove the grating lobes, the 6 dB-down regions were extended by a few nozzle diameters, i.e., several wavelengths, and the source strength density levels were higher (see Fig. 3 in Ref. 49). As such, it can be concluded that the shapes of the F-35B source reconstructions are adequate for estimating the extent of the frequency-dependent source regions.

The equivalent source reconstructions vary with engine condition. The 150% ETR results have the highest levels (maximum of 63 dB) with 100% and 75% each seeing a further decrease (maxima of 57 dB and 54 dB, respectively). This change in source level with ETR is consistent with the increased noise levels seen in Fig. 2. The general shapes of the source regions across frequency are similar for all three ETRs. However, both 100% ETR and 75% ETR show that the main energy distributions (seen in the 6 dB-down regions) are narrower above 200 Hz than the 150% ETR results are. For example, at 500 Hz, the region is approximately 8 m across at 150% ETR, closer to 5–6 m across at 100% ETR, and between 4 and 5 m across at 75% ETR with most of the decrease coming from the downstream side of the source region. The broader high-frequency source regions at 150% ETR are possibly related to effects of afterburning conditions. In addition to the overall trends seen by comparing ETRs, a closer look is needed to appreciate some details.

The source strength density maps in Fig. 4 also show apparent source locations for the multiple spectral peaks (seen in Fig. 2 and discussed in Sec. III B). The localization of the different peaks is most clearly seen at 100 Hz and 200 Hz near 13 m and 7 m, respectively. The peak around 300 Hz is harder to identify in the 150% ETR reconstruction, but it can be seen at 5 m in the 100% ETR construction. The positioning of the peaks in the source reconstructions combined with the 6 dB-down regions at these frequencies shows that the sources for the different peaks appear to originate in overlapping spatial regions both in front of and beyond the MARP (Fig. 1) with lower peak frequencies located farther downstream than higher frequency peaks. The source strength densities from the full array have been used to predict the sound field, and the results compare well to the sound levels measured.[63]

The full array results also contain a set of vertical striations, forming near 400 Hz at all three engine conditions. The striations are also clearly seen in both the HM and the GINV method results in Fig. 3(c). Perhaps these striations are indicative of shock cells that are critical in the formation of BBSAN as seen by their disappearance in the TMN subarrays discussed in Sec. IV E. These striations also appear in multisource statistically optimized near-field acoustical holography (M-SONAH) reconstructions on the same dataset, especially for 150% ETR, but are not quite as pronounced for other engine conditions (see Fig. 7 of Ref. 53). The upper frequency limit of the M-SONAH reconstructions

https://doi.org/10.1121/10.0001260

is also limited by grating lobes. Further investigation into these striations will require the application of UPAINT to remove the grating lobes to determine if they are indeed physical phenomena.

The source strength densities in Fig. 4 come from the diagonals of the SCSMs at each frequency. The complex SCSMs also contain information about coherence properties of the reconstructed sources. One measure that can be used to investigate frequency-dependent variation in source coherence is the coherence length, L_{γ^2}. Wall *et al.*[64] defines L_{γ^2} as the spatial distance from each reference point to the location where coherence drops below 0.5. The L_{γ^2} in the upstream direction are calculated for F-35B source reconstructions and displayed in Fig. 5. A general trend of shorter source with increasing frequency was observed across all engine conditions: L_{γ^2} exceeded 8 m below 60 Hz and transitioned to less than 1 m above 400 Hz. In addition, generally longer L_{γ^2} existed for near z = 10–15 m at frequencies below 200 Hz. These general trends confirm those shown for a tactical aircraft with different nozzle geometry.[49] (However, in Ref. 49, both the upstream and the downstream coherence lengths were calculated with the smaller of the two being displayed.)

While the L_{γ^2} can help identify trends in source coherence, comparison between the specific frequencies at which the multiple peaks occur is best facilitated by scaling L_{γ^2} by the wavelength. The standard coherence length values vary too rapidly across the wide range of frequencies to identify the specific features of the overlapping noise sources present in the reconstructions (Fig. 4). To combat this variance, a nondimensionalized coherence length was calculated; the original coherence lengths are divided by the wavelength, λ, as indicated by Swift *et al.*[52] The nondimensionalized coherence lengths as a function of frequency for the F-35B source reconstructions are shown in Fig. 5. The area shown is the same as that indicated by the −12 dB contour line in Fig. 4. This spatial aperture was chosen due to the significant uncertainty at lower levels.

Portions of the source region associated with spatio-spectral lobes appear to display slightly elevated nondimensionalized source coherence lengths. One striking feature is the large drop in source coherence which occurs above 500 Hz, likely due to the presence of two competing noise sources: TMN and BBSAN. (If the drop in self-coherence at these frequencies were due to grating lobes, it would likely affect the entire source region and not just the region that corresponds with the localization of BBSAN as shown in Sec. IV D). Below 150 Hz, the general increase in coherence length with z implies that the noise generation at these frequencies becomes more coherent farther downstream as was observed for a comparable aircraft in Ref. 49. While the general trend of increasing coherence with increasing z continues above 150 Hz, bands of shorter coherence lengths can be seen at all engine conditions. These lower coherence bands run at a slight diagonal (blue through the purple) at the downstream edge of the 12 dB-down region.

These coherence length trends coincide with the multiple spectral peaks in the source reconstructions that are

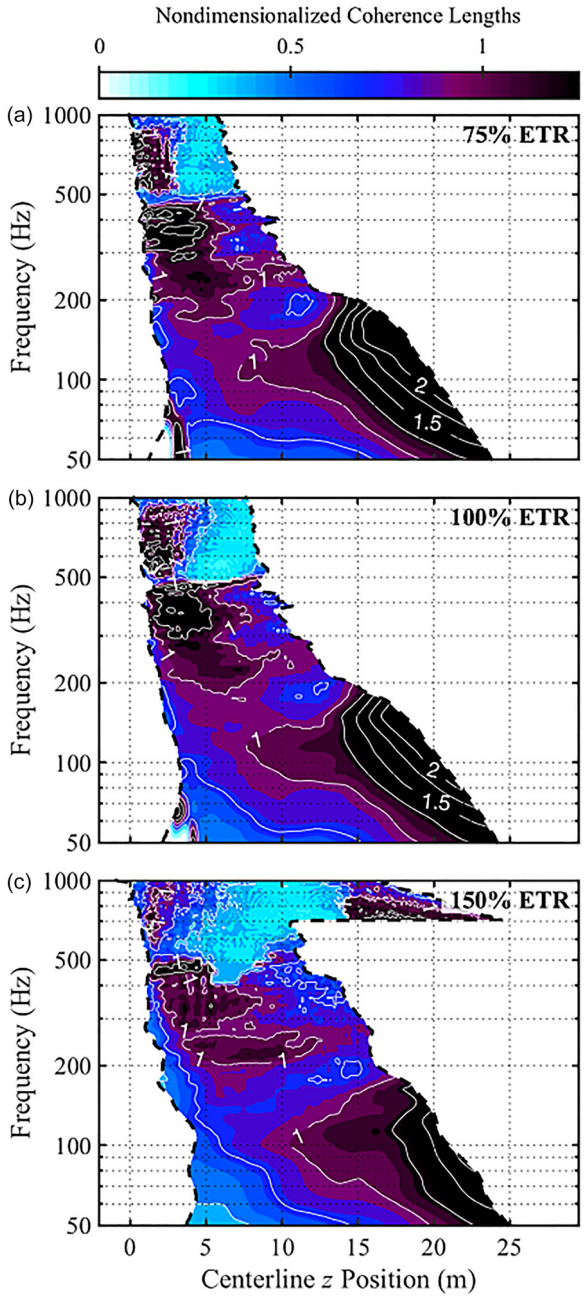

FIG. 5. (Color online) Source L_{γ^2} in the upstream direction calculated from the reconstruction cross-spectral matrix and normalized by λ for locations with source strength densities within 12 dB of the maximum at each frequency in Fig. 4 for the full array at (a) 75%, (b) 100%, and (c) 150% ETR.

present in the spectral maps and the reconstructions (approximately 100, 200, 300, and 400 Hz) in Figs. 2 and 4, as well as in Refs. 53 and 52. The regions of high coherence correspond to the same positions as the peaks in the reconstructions, and the bands of lower coherence correspond to the drops in source strength between the peaks. The bands of lower coherence appear to provide evidence that the sources of the individual lobes are not correlated but originate in overlapping regions. This idea is supported by a comprehensive correlation and coherence analysis on this same dataset by Swift*et al.*[52]

C. Subarray selection

To investigate the incoherence among different noise sources and obtain equivalent source distributions for each, the original 71-microphone array was divided into 3 subarrays. In Fig. 2, the dashed lines on the spectral plots indicate the extent of the three subarrays. The first subarray (18 microphones spanning 35°–75°, the "sideline subarray" in Fig. 1) is selected to isolate the BBSAN (see Fig. 3 in Ref. 13) without the dominating influence of TMN. The second subarray (30 microphones spanning 75°–120°, the "middle subarray" in Fig. 1) contains the spatially overlapping lobes and the majority of maximum noise region. The final subarray (23 microphones spanning 120°–153°, the downstream subarray in Fig. 1) includes mostly the largest, lowest frequency lobe with directivity farthest downstream. A preliminary study by Harker *et al.*[65] performed a division in line array measurements for a similar tactical aircraft and found that such a division adequately divided fine-scale and large-scale TMN via a mid-array and downstream array split. The division of a full array was further explored on the same dataset in Ref. 49, which found no evidence of BBSAN and used OTO band reconstructions to show a division of fine-scale TMN and large-scale TMN, which provides support for the divisions used in the current study. The source strength densities for each subarray are shown in Secs. IV D and IV E.

D. Sideline subarray results

The sideline array is chosen to estimate source regions of the BBSAN and the fine-scale TMN. The two-source model describing the generation of tactical aircraft noise[1] predicts that omnidirectional, fine-scale turbulent structure is detected to the side and forward of the MARP (Fig. 1). BBSAN propagates in this same region and is stronger than the fine-scale TMN[13] between 35° and 70°—the angular aperture spanned by the 18 element sideline subarray. The time-averaged, cross-spectral density matrix, **C**, at each frequency for the sideline subarray is input to the HM, and the resulting source strength densities are shown in Figs. 6(a), 6(b), and 6(c) for 75%, 100%, and 150% ETRs, respectively. These source reconstructions have a significantly different shape than when the full array was used (Fig. 4) and have levels much lower than those found in the full array.

A general trend across all engine conditions from the sideline subarray (Fig. 6) is the presence of three peak regions. These regions are most clearly seen in the 150% ETR case [Fig. 6(c)]: the first is below 100 Hz at $z = 5$ m, the second near 200 Hz and $z = 2$ m, and the third near 500 Hz. The white contour lines indicate their presence in the other engine conditions. The highest source levels are located between 400 and 600 Hz and given the levels and frequencies indicated by Vaughn *et al.*[13] show the equivalent acoustic source distributions of the BBSAN, whereas the peaks at lower frequencies are likely related to fine-scale TMN. The largest difference between these peaks—approximately 5 dB—occurs at 100% ETR [Fig. 6(b)]. The BBSAN

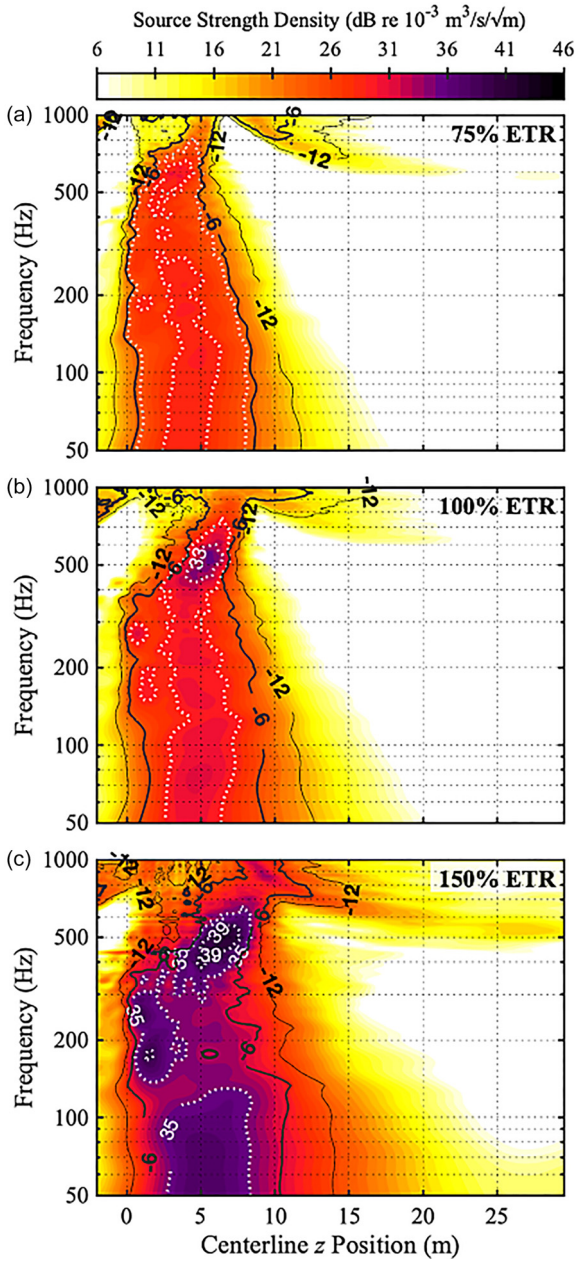

FIG. 6. (Color online) Source strength densities using the sideline subarray (18 microphones spanning 35°–70°), similar to Fig. 4; (a) 75%, (b) 100%, and (c) 150% ETR.

equivalent source distributions are substantially different than at lower frequencies because the location of the upstream edge of the 6 and 12 dB-down regions shift dramatically (approximately 4 m) at each engine condition. This shift is not present in the full array reconstructions in Sec. IV B, nor in the other subarrays in Sec. IV E. The main difference between these reconstructions and the others is that BBSAN is only dominant in the angular region spanned by this sideline subarray.[13]

From the source strength density maps obtained from the HM using the sideline array, the apparent origin of BBSAN initiates near $z = 3$ m at 400 Hz and shifts downstream slightly as frequency increases. While the

https://doi.org/10.1121/10.0001260

interpretation must be qualified with a reminder that grating lobes are present at these frequencies, removal of grating lobes via UPAINT for a comparable aircraft has shown that the 6 dB-down regions remain in relatively the same positions (varying by only a few nozzle diameters). Thus, the shift in the regions of the source distribution above 400 Hz is greater than the uncertainty due to the grating lobes, although the source strength density levels are likely underestimated.

Nondimensionalized coherence lengths also help verify the shift from TMN to BBSAN near 400 Hz. Over this sideline region, fine-scale TMN tends to dominate below approximately 300 Hz, and BBSAN covers 400–600 Hz as it varies across engine conditions as seen in the spectral decompositions shown by Neilsen *et al.*[4] and in the spectral maps in Fig. 2. Within the 12 dB-down regions shown in Fig. 7, the coherence lengths are fairly uniform with most regions having coherence lengths greater than half of a wavelength. Below 400 Hz, points where the coherence lengths decrease correspond to the increased source strength densities seen in Fig. 7. The shortest coherence lengths, on the other hand, are localized to the frequencies and position ascribed to the BBSAN. For example, in the 75% ETR plot, a region with nondimensionalized coherence lengths of approximately 0.25 is found around 2–5 m near 500 Hz. Similar spots can be seen in the 100% and 150% ETR plots at slightly lower frequencies. These areas most likely correspond to the spatial regions and frequencies where BBSAN and fine-scale TMN are competing, thus lowering the source coherence.

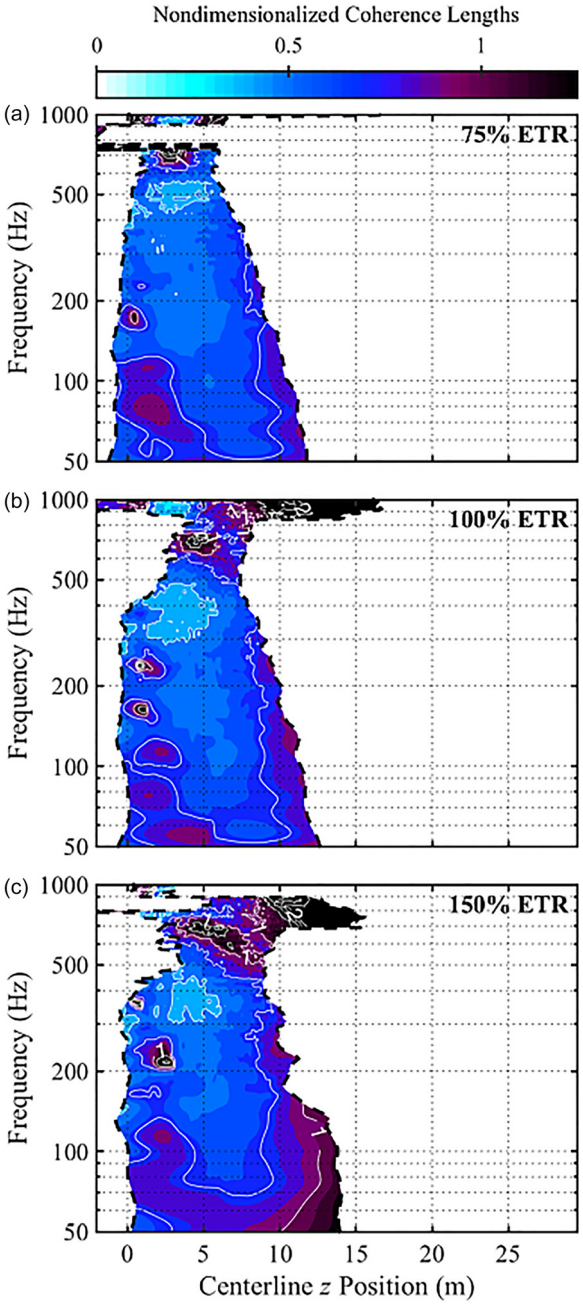

FIG. 7. (Color online) Source L_{γ^2} values calculated for the sideline subarray (18 microphones spanning 35°–70°), similar to Fig. 5.

E. Additional results

To investigate the source locations of different parts of the TMN without interference from BBSAN, the time-averaged cross-spectral matrices for the middle subarray (30 microphones spanning 75°–120°) and downstream subarray (23 microphones spanning 120°–153°) are each input into the HM. The resulting source strength densities using the middle subarray are shown in Fig. 8 and the downstream subarray is shown in Fig. 10 with the corresponding upstream, nondimensionalized coherence lengths in Figs. 9 and 11, respectively.

1. Middle subarray

The middle subarray results in Fig. 8 are similar to the full array results (Fig. 4). The upstream 6 dB-down edge retains the same general positioning across all frequencies and engine conditions as seen in the full array results, indicating that the middle subarray accounts for the majority of the source reconstructions when the full array is used. The same multiple spectral peaks at 100, 200, 300, and 400 Hz (discussed in Sec. IV B) are seen using the middle subarray input and localized in the same positions with the exception of the 100 Hz centered peak not extending as far into the lower frequencies. These middle subarray results confirm that the equivalent source distributions for the multiple peaks above 100 Hz overlap substantially as was indicated in prior studies.[51–53,64]

While the downstream edge of the 6 dB-down region for the middle subarray appears to follow the same trends as the full array at higher frequencies, the extent of the source distribution is significantly reduced at frequencies below 150 Hz with the downstream edge less by approximately 5 m or more. Both reductions at lower frequencies are expected since this subarray does not include as much of the lower frequency levels as can be seen by the division lines in Fig. 2. Other possible reasons for this include the splitting of the lowest frequency lobe and different families of Mach

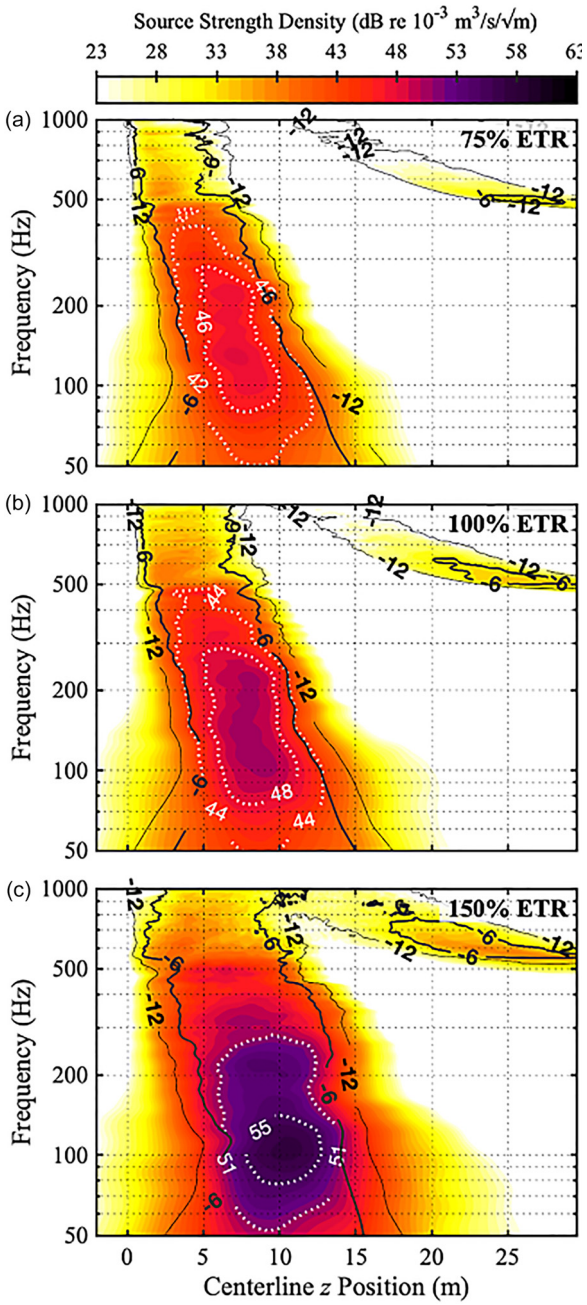

FIG. 8. (Color online) Source strength densities for the middle subarray (30 microphones spanning 75°–120°), similar to Fig. 4.

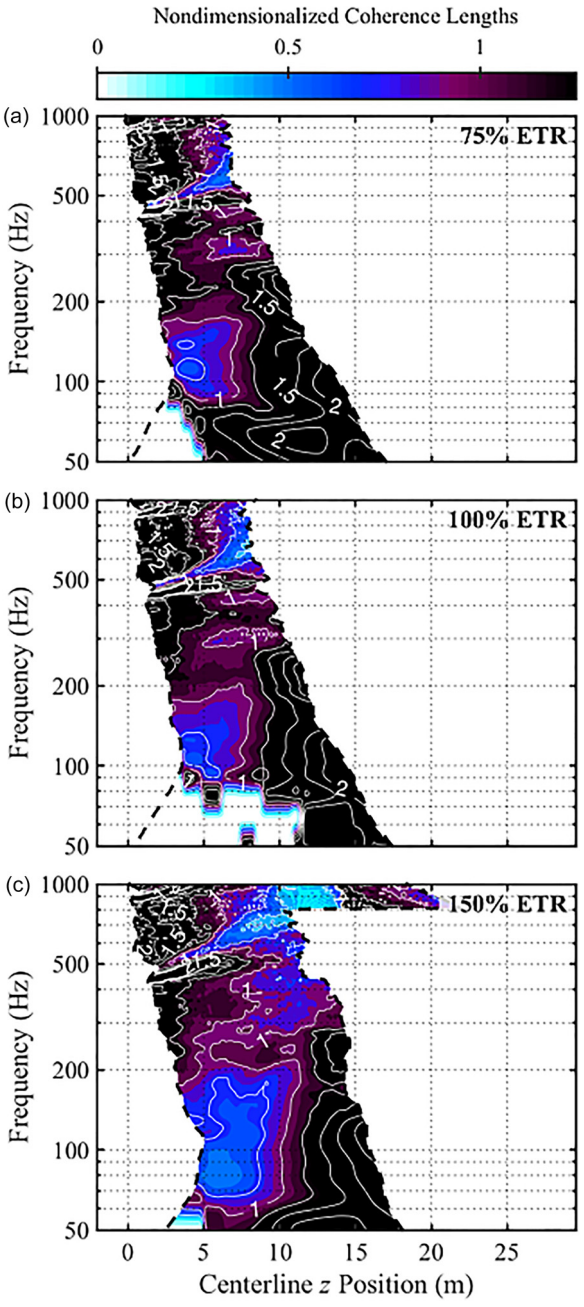

FIG. 9. (Color online) Source L_{γ^2} values calculated for the middle subarray (30 microphones spanning 75°–120°), similar to Fig. 5.

waves and the possibility that sound in the lowest frequency lobe may come from upstream.[66]

The middle subarray results, below 300 Hz, exhibit multiple peaks indicative of the TMN lobes. These different TMN lobes are similar to those in the full array results in Fig. 4 (and the spectral levels in Fig. 2). The location of the lowest frequency peaks (around 100 Hz) has been shifted slightly upstream, although their levels are slightly lower (approximately 1–3 dB). The second lobe (at around 200 Hz) is found in approximately the same location, and the levels are preserved (within 1 dB). These results show that the middle subarray captures most of the energy found in the spatiospectral lobes.

A curious difference between this middle subarray and the full array results (Fig. 4) is the disappearance of the striations above 500 Hz seen at all engine conditions. Upon removing the data captured by sideline subarray, the striations disappear across all engine conditions. In fact, the source strengths found when the middle and downstream subarrays were input together also did not contain the striations. This observation appears to contradict the potential cause of the striations being due to similar striations seen in the overall SPL measurements mentioned in Sec. III B (see Ref. 53, Fig. 2), as those striations occur in the data captured by the middle and downstream subarrays. However, the true cause of the striations cannot be

https://doi.org/10.1121/10.0001260

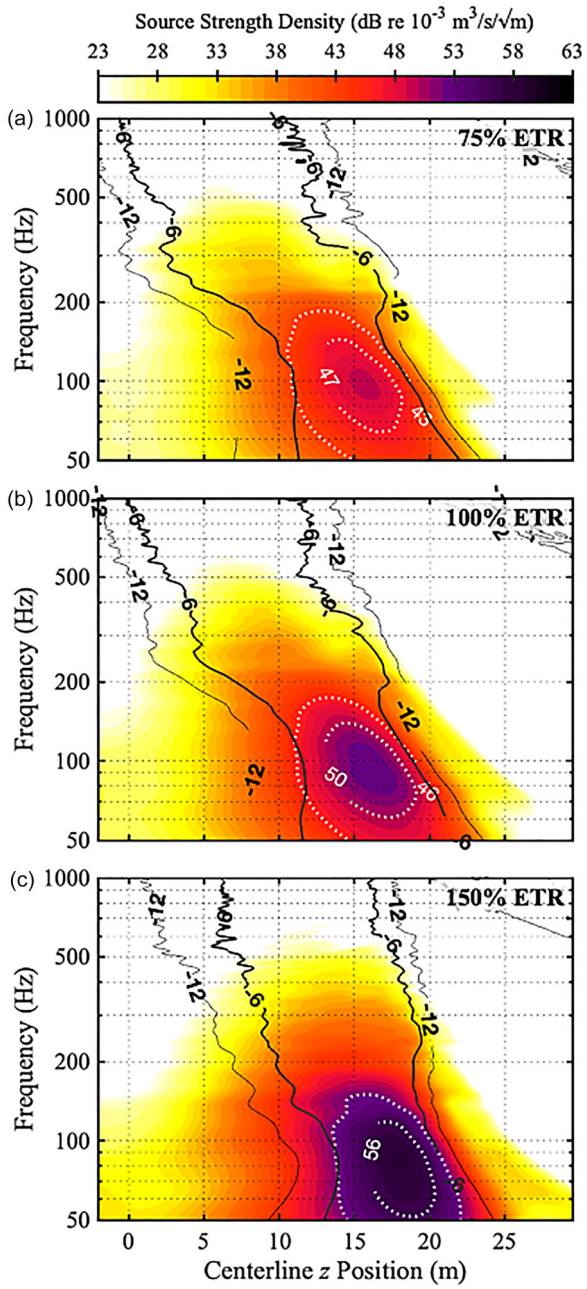

FIG. 10. (Color online) Source strength densities for the downstream subarray (23 microphones spanning 120°–153°), similar to Fig. 4.

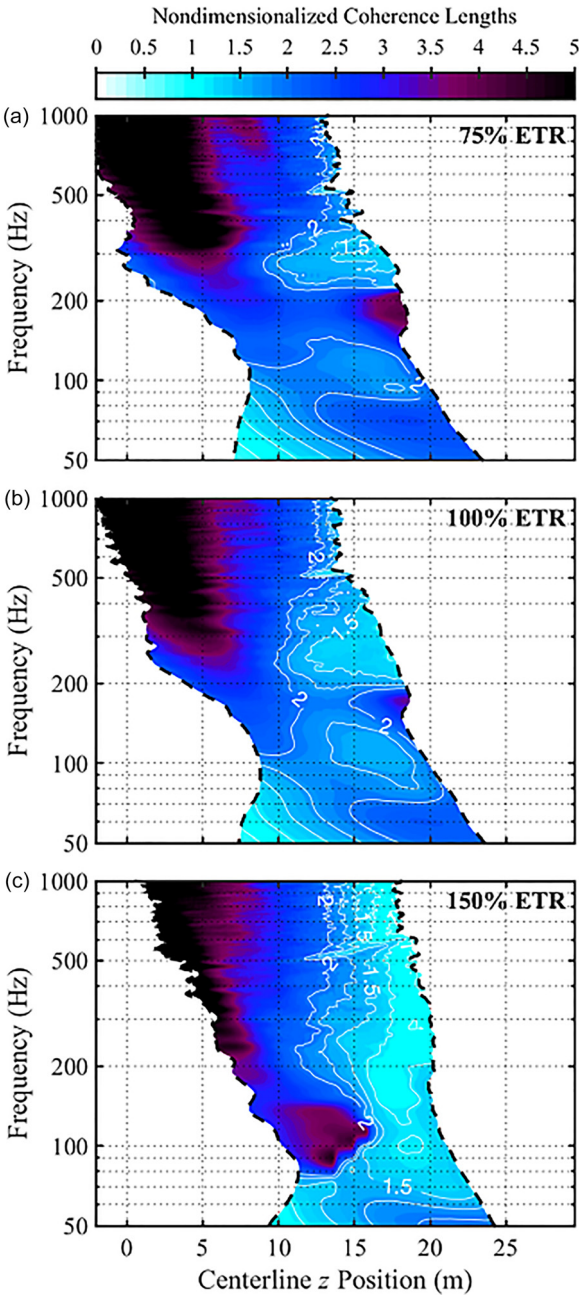

FIG. 11. (Color online) Source L_{γ^2} values calculated for the downstream region subarray (23 microphones spanning 120°–153°), similar to Fig. 5, except with a different scale to show the significantly longer coherence lengths.

confirmed until future work is done to remove the grating lobes.

The types of noise present in the middle subarray can be further examined by considering their corresponding upstream, nondimensionalized coherence lengths as shown in Fig. 9. In general, the coherence lengths for the middle subarray SCSMs are similar to those seen in the full array (Fig. 5), except the all-white areas below 100 Hz along the upstream edge are due to numerical artifacts introduced by using a smaller array. Downstream sources still have the highest coherence lengths with dips along this edge occurring at the same frequencies (300, 400, 500 Hz). However, the dip in coherence lengths previously seen at 200 Hz is almost nonexistent (with the exception of a tiny dip for 150% ETR). The conclusion that these dips are related to the overlapping generation of the multiple spectral peaks implies that the middle array did not capture much of the downstream sources for the 200 Hz lobe, which is consistent with the spectral content for the middle subarray shown in Fig. 2.

A significant difference between what is seen in this middle subarray and the full array is that the significant decrease in coherence length near and above 500 Hz (for all ETR) shown in Fig. 5 has almost entirely disappeared. This large drop was attributed to the competing nature of the fine-scale TMN and BBSAN, and its disappearance means

that the noise reaching this subarray is not influenced by these competing sources. There is still a dip at 150% ETR at the same frequencies and locations, and it could be attributed to large-scale TMN competing with fine-scale TMN at these frequencies or indicate that not all BBSAN was removed when selecting the subarray. However, grating lobes complicate drawing conclusions for drops in coherence length above about 500 Hz.

The variation in the multiple spectral peaks in the source strength densities from the middle array is quantified by comparing the location of the peaks and the extent of the 6 dB-down regions for the middle subarray at each ETR. The approximate frequencies of these multiple "lobes" can be seen in Fig. 2, are described in more detail in Refs. 53 and 52, and are listed in the first column of Table I. To demonstrate how each lobe's apparent source position changes across engine conditions, Table I also lists the location of the peak in the source strength density plots at each frequency (Fig. 8) and the width of the 6 dB-down regions. In all cases, 150% ETR has peak positions localized farther downstream than both 75% and 100% ETR with all but the first lobe also spanning a larger spatial extent. Given the increase of thrust exiting the nozzle as the ETR increases, this trend is expected.[67] Table I, combined with Fig. 8, provides clear evidence that for the F-35B, the multiple lobes all originate in overlapping regions.

2. Downstream subarray

The downstream subarray (23 microphones spanning 120°–153°) was selected to view the source locations of noises that primarily travel in the far aft direction. The reconstructed source levels, shown in Fig. 10, are vastly different than the previous results. In comparison to the full array (Fig. 4), the upstream 6 dB-down edges are shifted farther downstream consistently for all frequencies below 500 Hz. In Fig. 10(c), for 150% ETR at 100 Hz, that shift causes the upstream edge to change from $z = 1$ m to $z = 12$ m—a significant change. As for the downstream edge of the 6 dB-down region, below 150 Hz across all engine conditions, it moves farther downstream as frequency decreases and matches closely with the downstream edge of the full array results. Given the large peak at 100 Hz, the shift of the upstream 6 dB-down edge, and the consistent downstream 6 dB-down edge, it is clear that this subarray localizes the remainder of the main 100 Hz lobe seen in Fig. 2 and a portion of the 200 Hz lobe. As for frequencies above 200 Hz, the source levels decrease rapidly by 30 dB or more, indicating that the downstream subarray does not capture noise sources at those frequencies. The nondimensionalized coherence lengths in Fig. 11 show that below 300 Hz, the noise sources reconstructed by the downstream subarray are more coherent than the other two subarrays (note the change in the color scale). The long coherence lengths above 300 Hz are likely due to the low source levels and possible end fire effects. Thus, it is clear that the downstream subarray localizes the 100 Hz lobe across all engine conditions and one main type of noise is present in the area covered by this subarray.

TABLE I. Comparison of equivalent source distributions of the spectral peaks from the middle subarray (30 microphones spanning 75°–120°) for each ETR. The frequency of each lobe (from Fig. 2), the location of the peak in the source strength densities, and the extent of the 6 dB-down width are included.

	ETR	Frequency (Hz)	Peak position (z; m)	6 dB width (m)
Lobe 1				
	75%	100	8.35	7.55
	100%	100	8.85	7.65
	150%	100	10.3	7.6
Lobe 2				
	75%	200	6.85	6.4
	100%	200	8.1	6.6
	150%	200	10.3	8.45
Lobe 3				
	75%	350	4.3	5.45
	100%	300	6.2	6.6
	150%	300	7.8	9.45
Lobe 4				
	75%	500	2.4	6.05
	100%	500	5.7	6.75
	150%	400	8.2	9.05
Lobe 5				
	150%	500	6.3	6.65

V. CONCLUSION

To formulate distinct equivalent acoustic source distributions for TMN and BBSAN produced by a tactical aircraft, a source reconstruction via an advanced phased-array method, called the HM,[22] has been applied to acoustical measurements made near a tied-down F-35B. This study has confirmed that the HM is an appropriate phased-array method for tactical aircraft noise as recommended by the numerical study by Harker.[35] The HM has been applied to data from a 32 m long ground-based array, and the resulting source strength densities were compared to a prior study[49] on a different tactical aircraft showing many of the same source features. In addition to obtaining these equivalent source reconstructions, analysis of the nondimensionalized coherence lengths of the reconstructed sources have shown the presence of competing noise sources in overlapping spatial and spectral locations across engine conditions. Recently, these results have been used for field predictions that compare well with data measured both closer to and farther from the 71 element ground-based array.[63]

To further investigate the competing noise sources, the full array measurements were divided into three subarrays (the sideline, middle, and downstream regions) to isolate the noise associated with TMN and BBSAN,with BBSAN captured on the sideline subarray and the TMN captured on the middle and downstream subarrays. The resulting source strength density for each of the subarrays has provided insight into the source locations of both BBSAN and TMN. In the case of BBSAN, it was discovered that at frequencies of the BBSAN spectral peak, the resulting equivalent source distributions are relatively narrow and shift downstream with increasing frequency. However, these BBSAN sources

appear to compete with structures that generate fine-scale TMN as evidenced by a drop in self-coherence near 500 Hz.

When the HM was applied to the middle and downstream subarrays, the resulting equivalent source reconstructions had maximum values at about 5–10 m aft of the nozzle exit plane. The striking feature, which has not been seen in prior laboratory-scale studies, is the presence of multiple lobes in the source reconstructions. Each of the large-amplitude lobes are found at the same frequencies as seen in the spectral maps with the level decreasing as the frequency increases. This analysis has shown that the lobes appear to come from overlapping spatial source regions across all ETR, and the nondimensionalized coherence lengths indicate decreased coherence among each of the lobes. Comparisons of the source distributions obtained for the fine-scale TMN, large-scale TMN, and BBSAN suggest they originate from overlapping regions: the resulting broadband equivalent source distributions indicate that the apparent region of maximum sound generation for these three jet noise phenomena occur in close proximity.

Although equivalent source distributions for BBSAN and TMN for the F-35 noise have been found, further work can be done. As was mentioned previously, the UPAINT method[50] to extend the capabilities of the beamforming algorithm by reducing grating lobes was not applied. Applying UPAINT to these results could prove useful in identifying more certainty sources above 500 Hz. It would also bring more insight into the striations that were localized in the full array source distributions but were not apparent in subarray source distributions. Further analysis can be performed by dividing the subarrays further through conditional selection to localize sources seen in spectral maps. For example, to localize just one lobe, a hypothetical box could be drawn around the lobe's position and frequency in an attempt to isolate and focus on its source properties. Other considerations are multidimensional reconstruction areas as this study only focused on equivalent source distributions at the nozzle height along the jet centerline.

ACKNOWLEDGMENTS

The authors gratefully acknowledge funding for the measurements, which was provided through the F-35 Joint Program Office and U.S. Airforce Research Laboratory (USAFRL) through the Small Business Innovation Research Program and supported through a cooperative research and development agreement between Blue Ridge Research and Consulting, Brigham Young University, and the U.S. Air Force. Analysis funding was also provided by the Office of Naval Research (Grant No. N000141410494). D.F.V. was funded through the Brigham Young University College of Physical and Mathematical Sciences, as well as through a grant for undergraduate research from the Brigham Young University Office of Research and Creative Activities. The authors also thank Jacob Ward for helpful discussions. Distribution Statement A: Approved for public release; distribution unlimited. Cleared 11/12/2019; JSF19-908.

[1]C. Tam, M. Golebiowski, and J. Seiner, "On the two components of turbulent mixing noise from supersonic jets," in *Aeroacoustics Conference* (1996), p. 1716.
[2]C. K. Tam, K. Viswanathan, K. Ahuja, and J. Panda, "The sources of jet noise: Experimental evidence," J. Fluid Mech. **615**, 253–292 (2008).
[3]C. K. W. Tam and K. B. M. Q. Zaman, "Subsonic jet noise from nonaxisymmetric and tabbed nozzles," AIAA J. **38**(4), 592–599 (1983).
[4]T. B. Neilsen, A. B. Vaughn, K. L. Gee, S. H. Swift, A. T. Wall, J. M. Downing, and M. M. James, "Three-way spectral decompositions of high-performance military aircraft noise," AIAA J. **57**(8), 3467–3479 (2019).
[5]T. B. Neilsen, K. L. Gee, A. T. Wall, and M. M. James, "Similarity spectra analysis of high-performance jet aircraft noise," J. Acoust. Soc. Am. **133**(4), 2116–2125 (2013).
[6]M. Harper-Bourne and M. J. Fisher, "The noise from shock-waves in supersonic jets," AGARD **11**, 1–13 (1973).
[7]S. A. E. Miller and P. J. Morris, "The prediction of broadband shock-associated noise including propagation effects," Int. J. Aeroacoust. **11**(7-8), 755–781 (2012).
[8]T. D. Norum and J. M. Seiner, "Broadband shock noise from supersonic jets," AIAA J. **20**(1), 68–73 (1982).
[9]C.-W. Kuo, D. K. McLaughlin, P. J. Morris, and K. Viswanathan, "Effects of jet temperature on broadband shock-associated noise," AIAA J. **53**(6), 1515–1530 (2014).
[10]H. K. Tanna, "An experimental study of jet noise part II: Shock associated noise," J. Sound Vib. **50**(3), 429–444 (1977).
[11]P. K. Ray and S. K. Lele, "Sound generated by instability wave/shock-cell interaction in supersonic jets," J. Fluid Mech. **587**, 173–215 (2007).
[12]P. J. Morris and S. A. E. Miller, "Prediction of broadband shock-associated noise using Reynolds-averaged Navier-Stokes computational fluid dynamics," AIAA J. **48**(12), 2931–2944 (2010).
[13]A. B. Vaughn, T. B. Neilsen, K. L. Gee, A. T. Wall, J. Micah Downing, and M. M. James, "Broadband shock-associated noise from a high-performance military aircraft," J. Acoust. Soc. Am. **144**(3), EL242–EL247 (2018).
[14]B. J. Tester and K. R. Holland, "Estimating the sound power radiated by a nozzle-based source in a test cell using a phased array," in *21st AIAA/CEAS Aeroacoustics Conference* (2015), p. 2979.
[15]K. L. Gee, M. Akamine, K. Okamoto, T. B. Neilsen, S. Tsutsumi, S. Teramoto, T. Okunuki, and M. Cook, "Characterization of supersonic laboratory-scale jet noise with vector acoustic intensity," in *23rd AIAA/CEAS Aeroacoustics Conference* (2017), p. 3519.
[16]P. Jordan and T. Colonius, "Wave packets and turbulent jet noise," Ann. Rev. Fluid Mech. **45**, 173–195 (2013).
[17]Y. Khalighi, F. Ham, J. Nichols, S. Lele, and P. Moin, "Unstructured large eddy simulation for prediction of noise issued from turbulent jets in various configurations," in *17th AIAA/CEAS Aeroacoustics Conference (32nd AIAA Aeroacoustics Conference)* (2011), p. 2886.
[18]T. Suzuki, "A review of diagnostic studies on jet-noise sources and generation mechanisms of subsonically convecting jets," Fluid Dyn. Res. **42**(1), 014001 (2010).
[19]A. Towne, T. Colonius, P. Jordan, A. V. Cavalieri, and G. A. Bres, "Stochastic and nonlinear forcing of wavepackets in a Mach 0.9 jet," in *21st AIAA/CEAS Aeroacoustics Conference* (2015), p. 2217.
[20]Q. Leclere, A. Pereira, C. Bailly, J. Antoni, and C. Picard, "A unified formalism for acoustic imaging based on microphone array measurements," Int. J. Aeroacoust. **16**(4-5), 431–456 (2017).
[21]R. Merino-Martínez, P. Sijtsma, M. Snellen, T. Ahlefeldt, J. Antoni, C. Bahr, D. Blacodon, D. Ernst, A. Finez, and S. Funke, "A review of acoustic imaging methods using phased microphone arrays," CEAS Aeronaut. J. **10**(1), 197–230 (2019).
[22]T. Padois, P.-A. Gauthier, and A. Berry, "Inverse problem with beamforming regularization matrix applied to sound source localization in closed wind-tunnel using microphone array," J. Sound Vib. **333**(25), 6858–6868 (2014).
[23]R. P. Dougherty, "Beamforming in acoustic testing," in *Aeroacoustic Measurements* (Springer, New York, 2002), pp. 62–97.
[24]J. P. Erwin, P. Panickar, P. Vogel, and N. Sinha, "Acoustic source localization of rectangular jets using large eddy simulation with numerical phased arrays," in *52nd Aerospace Sciences Meeting* (2014), p. 0179.
[25]S. S. Lee and J. Bridges, "Phased-array study of dual-flow jet noise: Effect of nozzles and mixers," in *12th AIAA/CEAS Aeroacoustics Conference (27th AIAA Aeroacoustics Conference)* (2006), p. 2647.

[26]M. Lee and J. S. Bolton, "Source characterization of a subsonic jet by using near-field acoustical holography," J. Acoust. Soc. Am. **121**(2), 967–977 (2007).
[27]D. Long, "Jet noise source location via acoustic holography and shadowgraph imagery," in *14th AIAA/CEAS Aeroacoustics Conference (29th AIAA Aeroacoustics Conference)* (2008), p. 2888.
[28]S. R. Venkatesh, D. R. Polak, and S. J. A. J. Narayanan, "Beamforming algorithm for distributed source localization and its application to jet noise," AIAA J. **41**(7), 1238–1246 (2003).
[29]D. Papamoschou and A. Dadvar, "Localization of multiple types of jet noise sources," in *12th AIAA/CEAS Aeroacoustics Conference (27th AIAA Aeroacoustics Conference)* (2006), p. 2644.
[30]R. Schlinker, S. Liljenberg, D. Polak, K. Post, C. Chipman, and A. Stern, "Supersonic jet noise characteristics and propagation: Engine and model scale," in *13th AIAA/CEAS Aeroacoustics Conference (28th AIAA Aeroacoustics Conference)* (2007), p. 3623.
[31]A. T. Wall, K. L. Gee, T. B. Neilsen, D. W. Krueger, and M. M. James, "Cylindrical acoustical holography applied to full-scale jet noise," J. Acoust. Soc. Am. **136**(3), 1120–1128 (2014).
[32]A. T. Wall, K. L. Gee, and T. B. Neilsen, "Multisource statistically optimized near-field acoustical holography," J. Acoust. Soc. Am. **137**(2), 963–975 (2015).
[33]A. T. Wall, K. L. Gee, T. B. Neilsen, R. L. McKinley, and M. M. James, "Military jet noise source imaging using multisource statistically optimized near-field acoustical holography," J. Acoust. Soc. Am. **139**(4), 1938–1950 (2016).
[34]R. P. Dougherty, "Functional beamforming for aeroacoustic source distributions," in *20th AIAA/CEAS Aeroacoustics Conference* (2014), p. 3066.
[35]B. M. Harker, "Characterization of military aircraft jet noise using wavepacket analysis and other array processing methods," Dissertation, Brigham Young University, Provo, UT, 2017.
[36]T. Brooks and W. Humphreys, "Extension of DAMAS phased array processing for spatial coherence determination (DAMAS-C)," in *12th AIAA/CEAS Aeroacoustics Conference (27th AIAA Aeroacoustics Conference)* (2006), p. 2654.
[37]V. Fleury, J. Bulte, and R. Davy, "Determination of acoustic directivity from microphone array measurements using correlated monopoles," in *14th AIAA/CEAS Aeroacoustics Conference (29th AIAA Aeroacoustics Conference)* (2008), p. 2855.
[38]T. Yardibi, J. Li, P. Stoica, N. S. Zawodny, and L. N. Cattafesta III, "A covariance fitting approach for correlated acoustic source mapping," J. Acoust. Soc. Am. **127**(5), 2920–2931 (2010).
[39]T. Yardibi, J. Li, P. Stoica, and L. N. Cattafesta III, "Sparsity constrained deconvolution approaches for acoustic source mapping," J. Acoust. Soc. Am. **123**(5), 2631–2642 (2008).
[40]U. Michel and S. Funke, "Noise source analysis of an aeroengine with a new inverse method SODIX," in *14th AIAA/CEAS Aeroacoustics Conference (29th AIAA Aeroacoustics Conference)* (2008), p. 2860.
[41]P. A. Ravetta, R. A. Burdisso, and W. F. Ng, "Noise source localization and optimization of phased-array results," AIAA J. **47**(11), 2520–2533 (2009).
[42]T. Suzuki, "L1 generalized inverse beam-forming algorithm resolving coherent/incoherent, distributed and multipole sources," J. Sound Vib. **330**(24), 5835–5851 (2011).
[43]R. P. Dougherty, "Improved generalized inverse beamforming for jet noise," Int. J. Aeroacoust. **11**(3-4), 259–289 (2012).
[44]F. Presezniak, P. A. Zavala, G. Steenackers, K. Janssens, J. R. Arruda, W. Desmet, and P. Guillaume, "Acoustic source identification using a generalized weighted inverse beamforming technique," Mech. Syst. Signal Process. **32**, 349–358 (2012).
[45]P. Zavala, W. De Roeck, K. Janssens, J. Arruda, P. Sas, and W. Desmet, "Generalized inverse beamforming with optimized regularization strategy," Mech. Syst. Signal Process. **25**(3), 928–939 (2011).
[46]S. S. Lee and J. Bridges, "Phased-array measurements of single flow hot jets," in *11th AIAA/CEAS Aeroacoustics Conference* (2005), p. 2842.
[47]L. Brusniak, J. Underbrink, E. Nesbitt, D. Lynch, and M. Martinez, "Phased array measurements of full-scale engine exhaust noise," in *13th AIAA/CEAS Aeroacoustics Conference (28th AIAA Aeroacoustics Conference)* (2007), p. 3612.
[48]J. R. Underbrink, "Pletharrays for aeroacoustic phased array applications," in *21st AIAA/CEAS Aeroacoustics Conference* (2015), p. 2978.
[49]B. M. Harker, K. L. Gee, T. B. Neilsen, A. T. Wall, and M. M. James, "Source characterization of full-scale tactical jet noise from phased-array measurements," J. Acoust. Soc. Am. **146**(1), 665–680 (2019).
[50]C. B. Goates, B. M. Harker, T. B. Neilsen, and K. L. Gee, "Extending the bandwidth of an acoustic beamforming array using phase unwrapping and array interpolation," J. Acoust. Soc. Am. **141**(4), EL407–EL412 (2017).
[51]A. T. Wall, K. M. Leete, K. L. Gee, T. B. Neilsen, M. M. James, and R. L. McKinley, "Preliminary investigation of multilobe fighter jet noise sources using acoustical holography," in *23rd AIAA/CEAS Aeroacoustics Conference* (2017), p. 3520.
[52]S. H. Swift, K. L. Gee, T. B. Neilsen, A. T. Wall, J. M. Downing, and M. M. James, "Spatiotemporal-correlation analysis of jet noise from a round nozzle high-performance aircraft," in *2018 AIAA/CEAS Aeroacoustics Conference* (2018), p. 3938.
[53]K. M. Leete, A. T. Wall, K. L. Gee, T. B. Neilsen, M. M. James, and J. M. Downing, "Dependence of high-performance military aircraft noise on frequency and engine power," in *2018 AIAA/CEAS Aeroacoustics Conference* (2018), p. 2826.
[54]T. F. Brooks and W. M. Humphreys, "A deconvolution approach for the mapping of acoustic sources (DAMAS) determined from phased microphone arrays," J. Sound Vib. **294**(4-5), 856–879 (2006).
[55]T. K. Moon and W. C. Stirling, *Mathematical Methods and Algorithms for Signal Processing* (Prentice Hall, Upper Saddle River, NJ, 2000), Vol. 1.
[56]E. G. Williams, "Regularization methods for near-field acoustical holography," J. Acoust. Soc. Am. **110**(4), 1976–1988 (2001).
[57]B. M. Harker, T. B. Neilsen, K. L. Gee, M. M. James, and A. T. Wall, "Spatiotemporal correlation analysis of jet noise from a high-performance military aircraft," in *21st AIAA/CEAS Aeroacoustics Conference* (2015), p. 2376.
[58]M. M. James, A. R. Salton, J. M. Downing, K. L. Gee, T. B. Neilsen, B. O. Reichman, R. McKinley, A. T. Wall, and H. Gallagher, "Acoustic emissions from F-35 aircraft during ground run-up," in *21st AIAA/CEAS Aeroacoustics Conference* (2015), p. 2375.
[59]T. B. Neilsen, A. B. Vaughn, K. L. Gee, S. H. Swift, A. T. Wall, J. M. Downing, and M. M. James, "Inclusion of broadband shock-associated noise in spectral decomposition of noise from high-performance military aircraft," in *2018 AIAA/CEAS Aeroacoustics Conference* (2018), p. 3146.
[60]B. O. Reichman, K. L. Gee, T. B. Neilsen, S. H. Swift, and A. T. Wall, "Acoustic shock formation in noise propagation during ground run-up operations of military aircraft," in *23rd AIAA/CEAS Aeroacoustics Conference* (2017), p. 4043.
[61]K. L. Gee, V. W. Sparrow, M. M. James, J. M. Downing, C. M. Hobbs, T. B. Gabrielson, and A. A. Atchley, "The role of nonlinear effects in the propagation of noise from high-power jet aircraft," J. Acoust. Soc. Am. **123**(6), 4082–4093 (2008).
[62]C. K. Tam, "Supersonic jet noise," Ann. Rev. Fluid Mech. **27**(1), 17–43 (1995).
[63]J. A. Ward, K. M. Leete, K. L. Gee, D. F. Van Komen, T. B. Neilsen, A. T. Wall, M. Downing, and M. M. James, "Comparing two inverse array methods for source reconstructions of noise radiated from a high-performance jet aircraft," J. Acoust. Soc. Am. **144**(3), 1671–1671 (2018).
[64]A. T. Wall, M. D. Gardner, K. L. Gee, and T. B. Neilsen, "Coherence length as a figure of merit in multireference near-field acoustical holography," J. Acoust. Soc. Am. **132**(3), EL215–EL221 (2012).
[65]B. M. Harker, K. L. Gee, T. B. Neilsen, A. T. Wall, and M. M. James, "Phased-array measurements of full-scale military jet noise," in *20th AIAA/CEAS Aeroacoustics Conference* (2014), p. 3069.
[66]A. B. Vaughn, K. L. Gee, S. H. Swift, A. T. Wall, J. M. Downing, and M. M. James, "Beamforming of supersonic jet noise for crackle-related events," Proc. Mtgs. Acoust. **35**(1), 040003 (2018).
[67]C. K. W. Tam, A. C. Aubert, J. T. Spyropoulos, and R. W. Powers, "On the dominant noise components of tactical aircraft: Laboratory to full scale," J. Sound Vib. **422**, 92–111 (2018).